

EFFECTS OF PROCESSING STRATEGIES ON SURFACE QUALITY AND MECHANICAL PROPERTIES IN HYBRID ADDITIVE MANUFACTURING OF IN718 ALLOY

Tao Wang^{1,2}, Chao Wang^{1,2*}, Juanjuan Li^{1,2}, Wenxi Wang^{1,2}

¹State Key Laboratory of Mechanical Transmission for Advanced Equipment, Chongqing University, Chongqing, 400044, China 1

²College of Mechanical and Vehicle Engineering, Chongqing University, Chongqing, 400030, China 2

Abstract

Additive and subtractive hybrid manufacturing (ASHM) has achieved broad recognition as an emerging technology, facilitating the processing of intricate components with enhanced geometric precision and dimensional accuracy. A laser metal deposition (LMD)/grinding hybrid additive manufacturing process was utilized to produce In718 alloy thin-walled parts. The forming quality analysis, microstructure characterization and mechanical property testing of the In718 parts were carried out. The multi-response objective optimization results for belt grinding process parameters indicate that a surface roughness of 0.533 µm and a material removal rate of 175.853 mg/s can be simultaneously achieved with Vs = 15.726 m/s, Vw = 10 mm/s, and Fn = 14.204 N. The performance indexes of In718 alloy prepared by ASHM have improved in density, surface smoothness, and side roughness. The overall content of precipitated phases in the In718 alloy is limited, with the Laves phase primarily existing in the form of fine particles. The average microhardness of the In718 is 515.3 HV. In addition, the In718 turbine hollow blade was prepared through the optimized ASHM process, which verified the feasibility of the hybrid manufacturing system.

Keywords: In718 alloy, Laser Metal Deposition, Abrasive Belt Grinding, Additive and Subtractive Hybrid Manufacturing, Forming Quality

1. Introduction

Inconel718 superalloy (In718) exhibits excellent fatigue strength, high yield strength, and good thermal corrosion resistance. This alloy is used in the manufacture of engine rotors, wings, support structures, and pressure vessels [1]. With the rapid advancement of technology, the demand for laser metal deposition (LMD) technology to produce complex In718 structural components is increasing in the aviation sector. Traditional preparation methods are cumbersome and yield low output. Conversely, LMD technology involves irradiating metal powder with a high-energy laser beam to melt and deposit it along a specified trajectory, achieving near-net shaping of components. Generally, the surface quality of formed parts made by LMD is rough, and phenomena such as sticky powder and collapse may occur. Post-processing, such as milling and grinding, is required. Abrasive belt grinding technology, recognized for its flexibility and adaptability, offers benefits like low operating temperatures and effective vibration absorption due to its pliable nature. It significantly contributes to processing intricate surface contours, particularly for components with weak rigidity. Consequently, integrating LMD technology and abrasive belt grinding is deemed a complementary approach. This combination addresses the limitations of LMD technology, including suboptimal surface finish, prolonged forming periods, and compromised forming quality, while capitalizing on the superior surface quality afforded by abrasive belt grinding [2].

In the aspect of composite manufacturing process planning optimization, Chen et al. [3] developed a methodology for manufacturing a series of parts based on the provided dimensions of the base plate. Zhang et al. [4] developed a process planning method capable of achieving the final geometric size in a composite processing cycle for planar geometric characteristics of various materials. Basinger et al. [5] devised an advanced hybrid manufacturing process planning system centered on geometric features. The process planning generated by this system enhances processing efficiency by approximately 54 percent compared to the existing hybrid manufacturing strategy. He et al. [6] employed material utilization, manufacturing time, manufacturing cost, and structural complexity as evaluation indices to assess the composite manufacturability of parts. These evaluation indices guide the process selection of additive manufacturing, subtractive processing, and their alternation. Concerning the forming quality of hybrid manufacturing, Zhang et al. [7] achieved a 31.6% reduction in surface roughness by combining arc additive manufacturing technology with milling processes. Du et al. [8, 9] fabricated maraging steel by integrating laser powder bed melting technology and milling, improving surface morphology, geometric shape accuracy, and microhardness. Feldhausen et al. [10] created a hexagonal structure using composite manufacturing technology through both additive and subtractive processes. The findings indicate that composite manufacturing can reduce the overall processing time by 68% compared to the traditional additive manufacturing method, and the average relative elongation at break of the specimen is enhanced by 71%.

Literature suggests that current additive and subtractive composite manufacturing technologies have improved the forming accuracy and performance of parts to a certain extent. However, in processing combinations, subtractive processes are primarily based on CNC milling. Limited research on thin-walled parts made from In718 using the LMD/grinding hybrid process currently exists. Therefore, the microstructure and microhardness of In718 alloy produced by LMD and the LMD/grinding hybrid process were analyzed. The influence of processing strategies on the surface quality and mechanical properties of In718 thin-walled parts was studied. The formation and distribution of the Laves phase during the hybridization process were discussed. Finally, the application of additive/subtractive manufacturing technology successfully produced a thin-walled In718 blade with outstanding dimensional accuracy and surface finish. This achievement underscores the technology's potential versatility across diverse industries.

2. Methods and experiments

2.1 Materials

Gas-atomized spherical In718 powder (Feihuang Technology Co., Ltd.) was used, with a particle size distribution of 53 μ m to 150 μ m. The characteristics of the powder are shown in Fig. 1. Table 1 provides the primary chemical composition of the In718 powder. To prevent fracture of the bonding layer between the deposited specimen and the substrate during the abrasive belt grinding process, the substrate must have a similar thermal expansion coefficient and good wettability with the powder material. Therefore, an IN718 alloy sheet was chosen as the substrate.

Table 1 - Chemical composition of In718 powder.

Elements	Ni	Cr	Nb	Мо	Ti	Al	Fe
Content (wt. %)	50~55	17~21	4.75~5.5	2.8~3.3	0.65~1.15	0.2~0.8	Bal

2.2 Thin-walled parts fabricated by LMD/grinding hybrid process

Once half of the target height of the thin-walled part is deposited, the robotic abrasive belt grinding system initiates the first round of grinding on its upper surface. Following this, LMD continues until the thin-walled part reaches the target height. Once the LMD process for the thin-walled part is complete, a second round of abrasive belt grinding is performed on the side surface. The optimized LMD parameters were applied during the fabrication of the thin-walled parts. Additionally, the

optimized laser metal deposition parameters included a laser power of 240 W, a scanning speed of 9 mm/s, and a powder feeding rate of 1.55 g/min.

2.3 Characterization methods and Mechanical testing

The formed thin-walled parts were separated from the substrate using wire electrical discharge machining, and their relative density was measured using the Archimedes drainage method. An electric balance (JT3003D) with an accuracy of 1 mg was used to weigh the thin-walled parts. Prior to microstructure characterization, the surfaces were polished using SiC sandpaper and alumina suspension. Subsequently, the polished specimens were chemically etched in a solution containing 4 g CuSO4, 20 ml HCl, and 20 ml H2O for 20 seconds. Following etching, the specimens were rinsed with alcohol and dried. The microstructure of the formed thin-walled parts was then observed using an environmental scanning electron microscope (ESEM, Quattro S). Finally, the elemental composition of the observed phase was analyzed with an energy dispersive X-ray spectrometer (EDS). Hardness measurements were conducted on the specimen using an in-situ nanoindentation tester (Hysitron TI950 Tribodenter), applying an 8 mN load with a 10 s dwell time. Each specimen was measured three times, and the average value was recorded as hardness.

3. Abrasive belt grinding process optimization for thin-walled parts

3.1 Experimental scheme

Based on previous research on the process parameters of LMD, the optimal process parameter combination for forming IN718 alloy thin-walled parts was determined: laser power 240 W, scanning speed 9 mm/s, and powder feeding rate 1.55 g/min. Following the principles of the Box-Behnken analysis method in response surface methodology, the linear velocity of the abrasive belt (Vs), the feed speed of the robot arm (Vw), and the normal pressure (Fn) were considered as factors, while the surface roughness (Ra) and material removal rate (MRR) of thin-walled parts were regarded as response variables. The response surface analysis with three factors and three levels was conducted, comprising 17 groups of tests. Additionally, five sets of central trials were included for repeated trials to estimate errors. The test factors and levels for the belt grinding test of IN718 alloy are presented in Table 2.

Table 2 - Level of process parameters distribution of belt grinding.

Level	А	В	С	
	Levei	Vs/ m • s-1	Vw/ mm • s-1	Fn/ N
	-1	4	10	2
	0	6	17	4
	1	8	24	6

3.2 Experimental result

The grinding test was conducted based on the process parameters outlined in Table 2, and the corresponding test results are provided in Table 3.

Table 3 - Experiments and results using BBD.

	Pro	cess paramet	Result		
Number	Vs (m/s)	Vw (mm/min)	Fn (N)	Ra (µm)	MRR (mg/s)
1	12	17	12	0.6058	109.286
2	12	17	12	0.613	113.091
3	12	17	12	0.6261	110.091
4	12	17	12	0.5856	105.349
5	12	17	12	0.5783	102.99
6	8	24	12	1.2034	94.229
7	12	10	16	0.732	178.857
8	16	17	16	0.9638	213.131
9	16	17	8	1.0346	83.931
10	16	10	12	0.4508	139.029
11	8	10	12	1.1527	65.429
12	8	17	8	1.5506	51.177
13	8	17	16	1.1142	132.209
14	12	24	8	1.3941	87.6
15	12	10	8	1.1202	45.657
16	16	24	12	1.1532	162.103
17	12	24	16	1.1348	190.354

The central test results are displayed in Table 4, where the percentage error (PE) indicates the variability of the experimental values relative to their mean values. The percentage error of the five groups of experiments on surface roughness and material removal rate falls within the range of 5%, suggesting that the experimental results are reasonable and effective.

Table 4 - Reproducibility and percentage (%) error for Ra and MRR

	Vs (m/s)	Vw (mm/min)	En.	Ra (µm)		MRR (mg/s)	
Number			Fn (N)	Experimental value	PE (%)	Experimental value	PE (%)
1	12	17	12	0.6058	-0.67	109.286	1.03
2	12	17	12	0.613	-1.86	113.091	4.55
3	12	17	12	0.6261	-4.04	110.091	1.78
4	12	17	12	0.5856	2.68	105.349	-2.6
6	12	17	12	0.5783	3.89	102.99	-4.78

3.3 Response surface

The interaction between Vs-Vw and Vs-Fn is depicted in Figure 1. From the interactive response diagram of Vs-Vw (Fig. 1a), it can be observed that the minimum surface roughness occurs within the range of Vs ($14 \sim 16$ m/s) and Vw ($10 \sim 12$ mm/s) when Fn is maintained at the center value. When Vs is at a high value, Vw has a significant effect on surface roughness. Conversely, when Vw is at a

low value, Vs significantly affects surface roughness. From the interaction responsivity of Vs-Fn (Fig. 1b), it is evident that when Vw is held constant at the intermediate value, the surface roughness initially decreases and then increases with the increase of factors (Vs and Fn). The reason for this trend may be that increased Vs inhibits the thermoplastic deformation of the grinding surface. However, excessive Vs accelerates abrasive particle wear and reduces surface quality. Increasing Fn within a specific range increases the number of effective abrasive grains between the abrasive belt and the thin-walled parts, promoting a balanced and stable grinding process. However, excessive Fn causes high temperatures at the grinding contact surface and accelerates the wear of abrasive grains, resulting in increased surface roughness. Based on the interaction characteristics of Vs-Fn, the minimum surface roughness can be found in the ranges of Vs (13-15 m/s) and Fn (11-13 N).

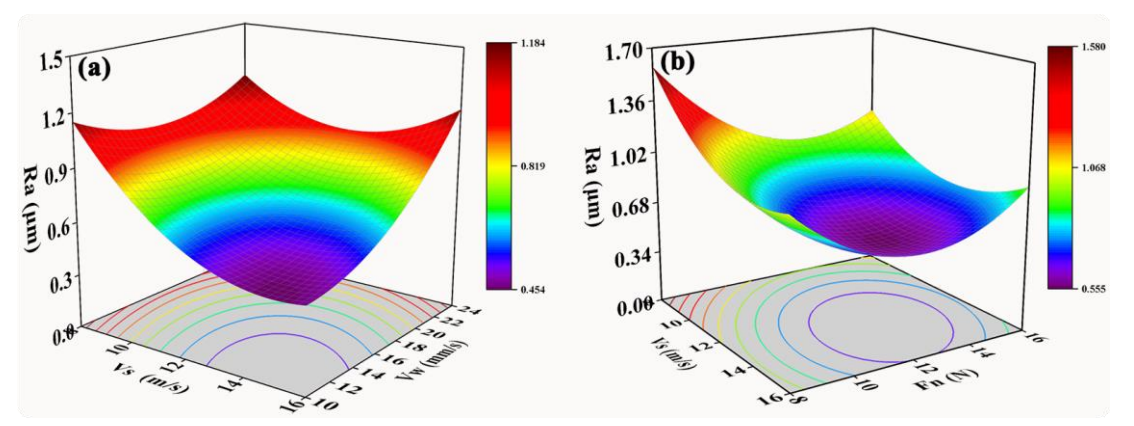


Figure 1 – Response surface showing the interactive effect of (a)Vs and Vw, (b) Vs and Fn on Ra.

Figure 2 shows the response surface illustrating the effect of Vs-Fn and Vw-Fn interactions on the material removal rate during abrasive belt grinding. Figure 2a indicates that Vs has little effect on the material removal rate at low Fn values. Conversely, at high Fn values, the effect of Vs on the material removal rate is significantly enhanced. The higher Fn increases the temperature of the grinding contact surface, softening the surface of the material formed, thus making it easier for the abrasive particles to remove the material. In Figure 2b, the effect of Fn on the material removal rate is more pronounced compared to Vs and Vw. This is primarily because the increase in Fn over time not only enlarges the effective contact area between the abrasive belt and the surface of the thin-walled part but also enhances the cutting depth of the abrasive particles [11]. Therefore, a higher Fn value can be selected from within the parameter range to achieve a high material removal rate in abrasive belt grinding.

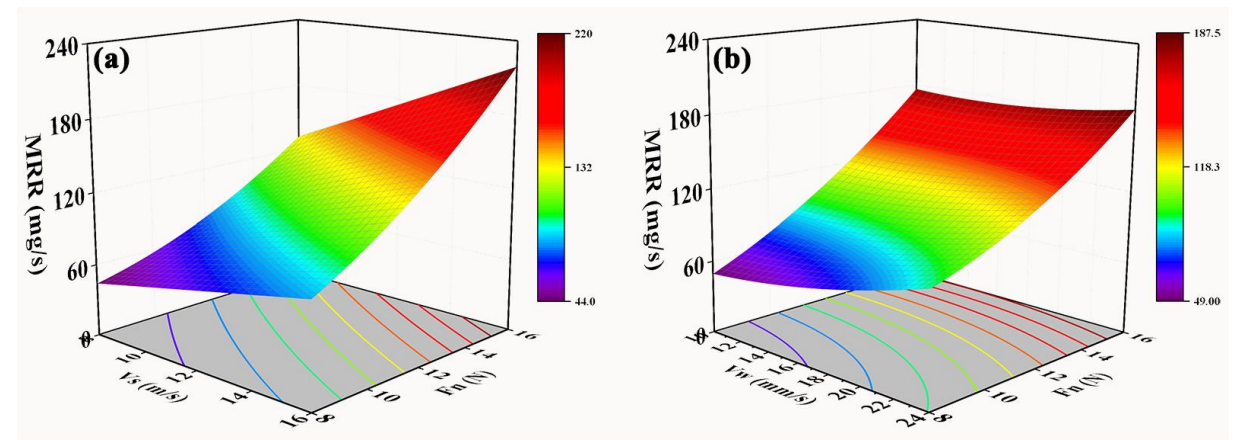


Figure 2 – Effect of different forming manufacturing methods on density (a); side surface roughness (b) and surface profile binary diagram and contour fitting curve (c).

3.4 Multi-objective optimization

The multi-objective optimization of Ra and MRR is conducted using the expectation function method. The expected values of these two responses are normalized, as shown in equations (1) and (2).

$$\begin{split} d_{Ra} = & \begin{cases} (\frac{U_{i} - F_{Ra}(A, B, C)}{U_{i} - L_{i}})^{t} & \text{if } L_{i} \leq F_{Ra}(A, B, C) \leq U_{i} \\ 0 & \text{if } F_{Ra}(A, B, C) > U_{i} \end{cases} \\ d_{MRR} = & \begin{cases} (\frac{1}{M_{RR}(A, B, C) - L_{i}})^{t} & \text{if } L_{i} \leq F_{MRR}(A, B, C) \leq U_{i} \\ U_{i} - L_{i} & \text{if } F_{MRR}(A, B, C) \leq U_{i} \end{cases} \\ 1 & \text{if } F_{MRR}(A, B, C) > U_{i} \end{cases} \end{split}$$
 (2)

$$d_{MRR} = \begin{cases} (\frac{F_{MRR}(A, B, C) < L_{i}}{F_{MRR}(A, B, C) - L_{i}})^{t} & \text{if } L_{i} \le F_{MRR}(A, B, C) \le U_{i} \\ 1 & \text{if } F_{MRR}(A, B, C) > U_{i} \end{cases}$$
(2)

In the formula, dRa - the expected value of the minimum surface roughness; dMRR - the expected value of the maximum material removal rate; Ui-upper limit value; Li-lower limit value; t- weight.

The process parameters of single and multi-objective optimization, along with the limiting conditions of response, are shown in Table 5. The optimization results are presented in Figure 3. For the singleobjective optimization aimed at minimizing Ra, the model predicts a value of 0.45 µm. Additionally, the expected value reaches 1, indicating high feasibility. The results of the single-objective optimization of the maximum MRR show a predicted value of 223.695 mg/s. For the multi-objective optimization of the minimum Ra and the maximum MRR, the model obtains predicted values of 0.533 µm for Ra and 175.853 mg/s for MRR, with a comprehensive response value reaching 0.853.

Table 5 - The limitations for process parameters and responses.

Parameter	Objective	Lower limit value (Li)	Upper limit value (Ui)	Weight (t)	Importance degree (ri)
Vs (m/s)	Within the set range	8	16	1	3
Vw (mm/s)	Within the set range	10	24	1	3
Fn (N)	Within the set range	8	16	1	3
Ra (µm)	Single target minimum	0.4508	1.5506	1	3
MRR (mg/s)	Single target maximum	45.657	213.131	1	3
Ra (µm)	multi-objective	0.4508	1.5506	1	5
MRR (mg/s)	optimization	45.657	213.131	1	3

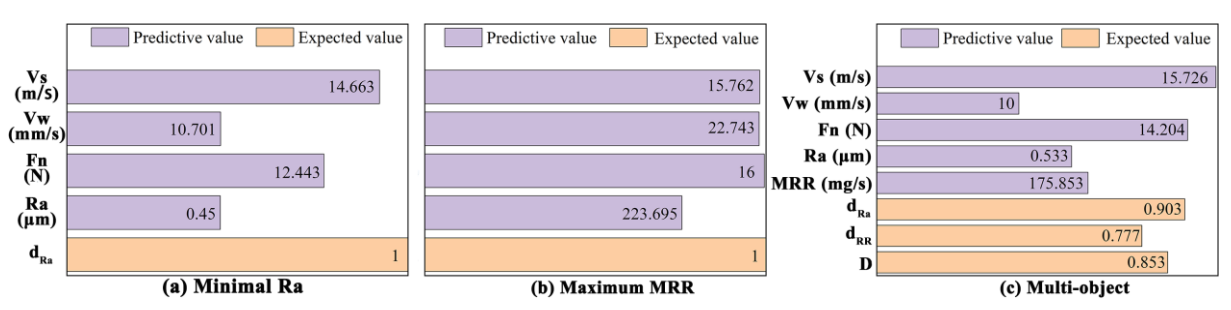


Figure 3 – Optimization goals for (a) minimal Ra, (b)maximum MRR and (c) multi-object.

3.5 Experimental verification of optimization result

The abrasive belt grinding experiment adopts the parameter combination for minimum Ra and maximum MRR, where Vs is 15.726 m/s, Vw is 10 mm/s, and Fn is 14.204 N. After abrasive belt grinding, the surface roughness of IN718 alloy prepared by laser metal deposition is 0.56055 μ m, and the material removal rate is 177.5 mg/s. The experimental results closely align with the multi-objective optimization results. The model prediction errors were 5.17% and 0.94%, respectively, verifying the model's reliability.

Figure 4a shows that the surface of the IN718 alloy has approximately parallel furrow-like stripes, with ductile cutting marks on both sides of the stripes. During the grinding process, the diamond abrasive particles are in close contact with the surface of the material and ploughing occurs, causing severe plastic deformation on the surface of the material. This deformation results in the removal of material with significant plastic deformation by grinding, leading to the formation of wear debris. Simultaneously, another portion of the material undergoes continued deformation perpendicular to the grinding direction, forming a convex stripe. Figure 4b shows the local magnification of region A in Figure 6a. The furrows (with a width of 10.7 μ m) and stripes are generated on the surface of the IN718 alloy by ploughing. The grinding surface stripes of the IN718 alloy were detected using EDS, and the results are presented in Figure 4c. Analysis of the O element distribution diagram reveals a significant increase in oxygen intensity at the stripe band, suggesting severe oxidative wear during the grinding process.

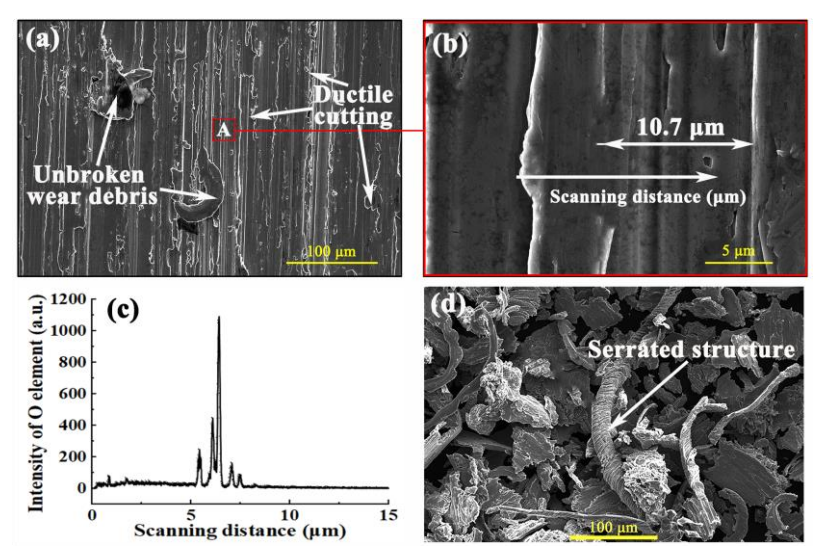


Figure 4 – (a) Surface morphology of IN718 alloy prepared by laser metal deposition after belt grinding; (b) is the microstructure enlargement diagram of the A region; (c) The EDS line scan results of the stripe band; (d) Wear debris morphology of IN718 alloy.

Figure 4d illustrates the morphology of the wear debris of the IN718 alloy under multi-objective optimization of grinding parameters. Two distinct morphological characteristics of the wear debris are observed. There are blocky debris and banded debris. Among these, the slender banded wear debris exhibits consistency with the shape of the unbroken wear debris depicted in Fig. 4a. This difference in morphology may be attributed to the uneven distribution of internal structure and hardness within the IN718 alloy [12]. When the material surface undergoes grinding shear force, ductile cutting is more prone to occur in regions with low hardness or high plasticity, resulting in the formation of long strips and irregular flake wear debris. Furthermore, a serrated structure was observed on the long strip wear debris, suggesting adiabatic shear on the surface of the IN718 alloy during the grinding process [13].

3.6 Surface layer microhardness

Figure 5 illustrates the microhardness distribution of the surface layer of the IN718 alloy along the depth from the grinding surface after the grinding experiment. Figure 5a illustrates a significant work-hardening phenomenon in the IN718 alloy after abrasive belt grinding, with work-hardening layer depths of approximately 40 μ m and 80 μ m, respectively. The average microhardness of the grinding surface of the IN718 alloy is 535.7 HV, while the average microhardness of the internal

substrate is 443.9 HV. As a result, the degree of work-hardening reached 120.69%.

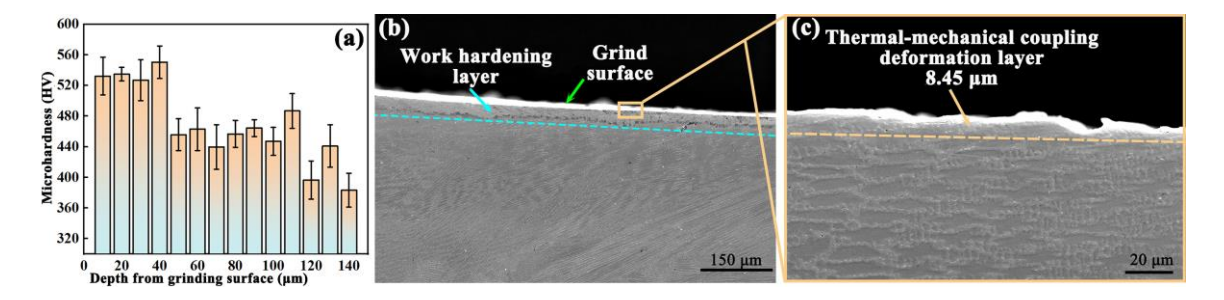


Figure 5 – (a) Microhardness distribution of IN718 alloy cross section; (b) Micrograph of grinding metamorphic layer of IN718 alloy; (c) is the local enlarged graph of the rectangular region (b).

Figure 5b illustrates a significant grain refinement phenomenon in the area (work-hardening layer) approximately 40 µm away from the grinding surface, aligning with the depth at which the surface microhardness exhibits a mutation. Figure 5c shows a thermal-mechanical coupling influence layer with a thickness of 8.45 µm on the grinding surface. In addition, when the surface roughness exceeds a critical value, the fatigue strength of the material decreases as surface roughness increases. When surface roughness is below this critical value, the fatigue strength of the material increases with the thickness of the hardened layer [14]. Therefore, to enhance the fatigue strength of IN718 alloy post-belt grinding, minimizing surface roughness on the grinding surface and increasing the thickness of the work-hardening layer should be considered.

4. Effect of processing strategy on manufacturing quality

Figure 6a shows the influences of different processes, including LMD and ASHM, on the density of thin-walled parts. The density of thin-walled parts prepared by LMD and ASHM is 97.86 % and 98.96 %, respectively, indicating enhanced density by optimizing process parameters. The belt grinding method can eliminate defects such as pores and cracks during LMD, improving part density. Figure 6b shows that the average surface roughness of the side surfaces of the thin-walled parts formed by the two methods is 3.82µm and 0.48µm, respectively. The side surface roughness of the ASHM specimen is smaller than that of the LMD specimen, indicating that ASHM can effectively remove the laser metal deposition texture from the side surface of the thin-walled part, thereby significantly improving its surface finish. As shown in Figure 6c, the surface contour of the thin-walled parts prepared by ASHM is relatively smooth during the robot's acceleration at the initial state, with a relatively small overall contour change amplitude. Profile curves obtained from the upper surface contour of two thin-walled parts are fitted to accurately compare the two contours' differences. The standard deviation of the fitted curves for two contours is 6.5 and 5.22. The surface contour flatness increases to 19.6%.

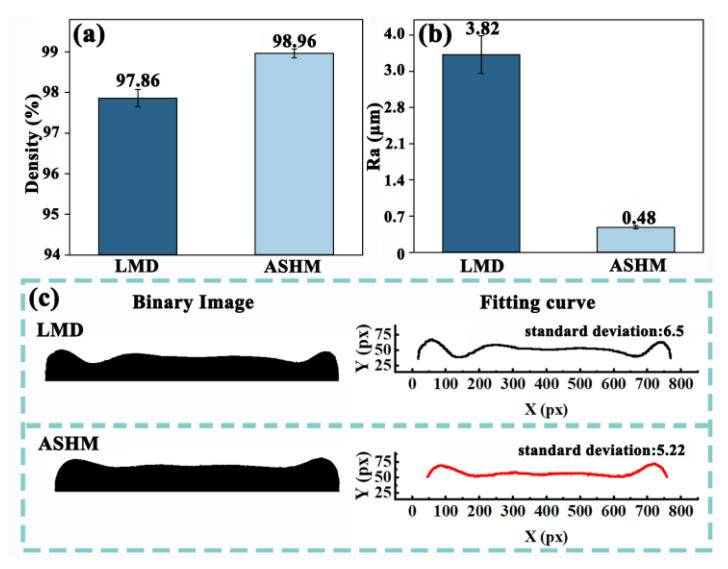


Figure 6 – Effect of different forming manufacturing methods on density (a); side surface roughness (b) and surface profile binary diagram and contour fitting curve (c).

5. Microstructure and microhardness

5.1 Microstructure

Figure 7 shows the microstructures of thin-walled parts fabricated by LMD and ASHM. The thinwalled parts consist of dendrite regions with dark contrast and interdendritic regions with light contrast. The interdendritic regions of thin-walled parts prepared by LMD are noticeably more developed than the interdendritic regions of specimens prepared by ASHM. EDS results (see Table 6) from 1 and 4 points show the existence of the y phase in interdendritic regions. In contrast, the dendrite regions are rich in Nb elements with a slight presence of Mo element, indicating the precipitation of the Laves phase. The segregation phenomenon is often discovered in IN718 alloy fabricated using additive manufacturing technology. The reason is that the characteristics of the rapid cooling process can quickly induce elemental segregation of atoms with a large diameter [15]. Some small granular phases (point 3 and point 6) are also found in the interdendritic regions. These small granular phases are identified as NbC based on the EDS results. Overall, the interdendritic regions are rich in a large amount of the Laves phase and a small amount of the NbC phase due to the shorter cooling time suppressing the formation of the NbC phase [16].

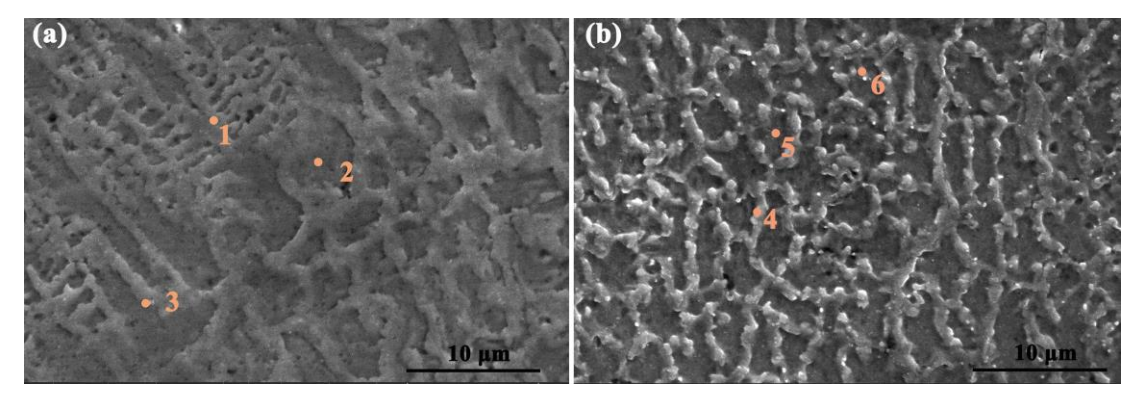


Figure 7 – Characterization results of SEM. (a) SEM map of LMD, (b) SEM map of ASHM.

	Table 6 - Mass distribution of elements in different phases					
	1	2	3	4	5	6
С	3.93	3.73	4.03	4.18	2.81	6.06
Ti	1.3	0.96	1.48	1.61	0.9	2.61
Cr	19.31	19.62	18.87	18.56	19.81	18.21
Fe	20.08	21.22	19.05	18.42	21.69	18.42
Ni	46.52	48.38	46.66	46.11	49.64	42.12
Nb	5.62	3.22	6.46	7.72	2.56	9.45
Мо	3.26	2.87	3.45	3.41	2.59	3.13

5.2 Microhardness

Figure 8 presents a comparative analysis of the hardness variations in thin-walled components fabricated using LMD and ASHM across different deposition heights. As the deposition height increases, the alteration in hardness for ASHM thin-walled components is inconspicuous, whereas the hardness values for LMD thin-walled parts exhibit significant fluctuations. These findings suggest that implementing ASHM in the forming processes is particularly advantageous for achieving a homogeneous hardness distribution in the resulting components. Moreover, the mean hardness value of thin-walled parts produced through ASHM (515.3 HV) exceeds that of counterparts manufactured via LMD (457.1 HV). This phenomenon primarily arises from two key factors. Firstly, the density of the thin-walled parts experiences a discernible enhancement subsequent to laser deposition and abrasive belt grinding. Cui et al. [17] reported that higher

density theoretically corresponds to elevated hardness characteristics. Secondly, the laser metal deposition process induces a relatively substantial precipitation of the Laves phase. The formation of the Laves phase necessitates a substantial quantity of Nb element, consequently impeding the development of the reinforcing phase γ'' . Ultimately, this process results in a decline in hardness. Furthermore, the mean hardness of thin-walled components fabricated through LMD and ASHM surpasses that of the substrate (395.9 HV), primarily attributable to the laser metal deposition process. Research indicates that laser additive manufacturing can notably refine grain structures and enhance microhardness [9].

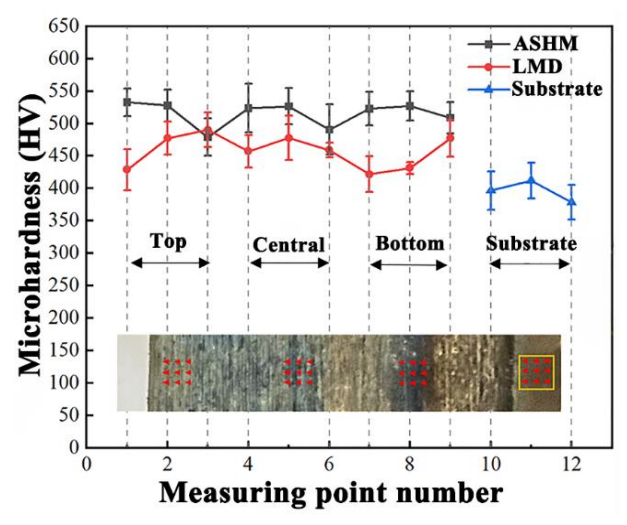


Figure 8 – Hardness of deposited thin-walled parts with different forming manufacturing methods.

6. Hollow thin-walled parts fabrication via LMD/grinding hybrid process

6.1 Forming strategy

The simplified three-dimensional model of the hollow turbine blade is depicted in Figure 9. The dimensions are 60 mm in length and 52 mm in height, and the wall thickness is 1.5 mm. The forming strategy for the hollow blade model is as follows: Initially, LMD forming is performed following the blade contour trajectory. Once a certain height is achieved, the hollow blade is subjected to abrasive belt grinding to flatten its upper surface. Secondly, determine if the deposition height meets the design specifications. Suppose it does not continue the alternating process of laser metal deposition and abrasive belt grinding. If it does, proceed with abrasive belt grinding on the side surface of the hollow blade. To expedite the processing of the flat upper surface of the hollow blade, the maximum MRR process parameters are employed for abrasive belt grinding. Additionally, to ensure both machining efficiency and surface quality of the hollow blade side surface, the combination of minimum Ra and maximum MRR process parameters is employed for grinding.



Figure 9 – Hardness of deposited thin-walled parts with different forming manufacturing methods.

6.2 Trajectory planning

Due to the complexity of the hollow blade surface, programming with a robot teaching pendant is inefficient and does not meet the accuracy requirements for additive manufacturing and abrasive belt grinding. Therefore, offline programming realizes the simplified hollow turbine blade model formed by ASHM. The hollow blade model is sliced using Cura open-source software for the additive manufacturing process. The software configures parameters, such as a 50% overlap rate and a Z-axis lift of 0.21 mm. The scanning path is specified as a border + 'Z' trajectory. Subsequently, the program is exported to the Karel programming language. The UG secondary development software is utilized for the subtractive manufacturing process to extract the point information of the hollow blade model's grinding trajectory. Subsequently, MATLAB software is used to convert to G-code. Finally, the formation of a hollow blade model is achieved by alternately employing additive and subtractive procedures.

6.3 Hollow blade model forming experiment

The morphology of the hollow blade formed by ASHM is depicted in Figure 10a. The surface of the formed part is smooth, and the texture phenomenon of the deposition layer has been eliminated. The average roughness of the side surface of the formed part is 0.586 µm, which closely matches the result of the multi-objective optimization for side surface roughness (with an error percentage of less than 10%), thus verifying the reliability of the multi-objective optimization model. The contour size information of the hollow blade is captured using a blue light three-dimensional scanner, and the blade model is reconstructed based on the captured data. The contour comparison between the reconstructed model and the original model is depicted in Figure 10b. The reconstructed model (in purple) closely matches the original model (in blue) in the primary area, indicating that the forming accuracy nearly meets the design requirements. The above results demonstrate that ASHM can achieve the forming of complex components and ensure high shape accuracy of the formed parts.

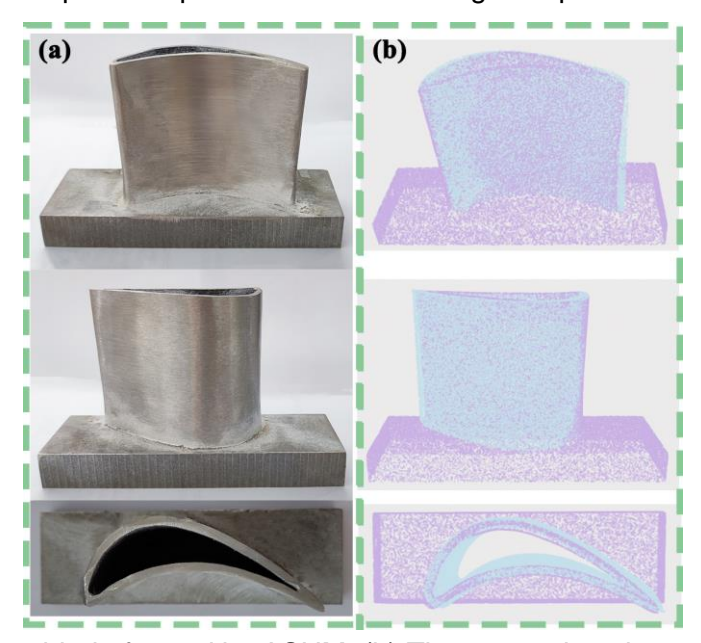


Figure 10 – (a) Hollow blade formed by ASHM, (b) The comparison between the formed hollow blade and the original model.

7. Conclusion

This study introduces a novel approach, the direct laser deposition/abrasive belt grinding hybrid manufacturing process (ASHM), for producing thin-walled In718 parts. The influence of processing strategy on the microstructure and mechanical properties of In718 thin-walled parts was studied. Additionally, the application verification of ASHM for curved hollow thin-walled parts was conducted. The key findings are as follows.

(1) The results of multi-response optimization of belt grinding parameters for LMD-fabricated In718 thin-walled parts reveal that achieving a surface roughness of 0.533 µm and a material removal rate

of 175.853 mg/s is feasible with Vs = 15.726 m/s, Vw = 10 mm/s, and Fn = 14.204 N. Furthermore, the grinding surface of IN718 alloy exhibits significant work-hardening, with a work-hardening layer depth of about 40 μ m and a grinding surface roughness of 0.561 μ m.

- (2) When compared with the LMD manufacturing method, ASHM demonstrates its superiority in forming indexes such as density, upper surface flatness, and side surface roughness. The thin-walled parts manufactured by both processes primarily consist of the base γ phase, Laves phase, and a small amount of NbC phase.
- (3) The thin-walled parts manufactured by ASHM, a method that significantly enhances the manufacturing process, achieved an average hardness of 515.3 HV, surpassing those of LMD specimens. Furthermore, the ASHM method successfully facilitated the manufacturing of curved hollow thin-walled parts, validating the feasibility of laser metal deposition/abrasive belt grinding hybrid manufacturing.

8. Contact Author Email Address

Corresponding Author: Chao Wang.

Email: c.wang@cqu.edu.cn.

Phone: +86 15213159822.

Fax number: +86 2365106195.

Name(s) of all other authors:

Tao Wang: wangtaocd@cqu.edu.cn, Juanjuan Li: 20210701012@stu.cqu.edu.cn, Wenxi Wang:

wx.wang@cqu.edu.cn.

9. ACKNOWLEDGMENTS

This work is financially supported by the National Natural Science Foundation of China (Grant No. 52375408).

10. Copyright Statement

The authors confirm that they, and/or their company or organization, hold copyright on all of the original material included in this paper. The authors also confirm that they have obtained permission, from the copyright holder of any third party material included in this paper, to publish it as part of their paper. The authors confirm that they give permission, or have obtained permission from the copyright holder of this paper, for the publication and distribution of this paper as part of the ICAS proceedings or as individual off-prints from the proceedings.

References

- [1] Hosseini, E, and Popovich, V. A. A Review of Mechanical Properties of Additively Manufactured Inconel 718. *Additive Manufacturing*, vol 30: pp 2019.
- [2] Zhou, H, Yang, Y. Q, Han, C. J, Wei, Y, Liu, Z. X, Tai, Z. H, Zhang, S. Q, and Wang, D. Laser Directed Energy Deposition/Milling Hybrid Additive Manufacturing of Thin-Walled Gh4169 Alloy: Effect of Processing Strategy on Its Microstructure and Mechanical Properties. *Materials Science and Engineering: A*, vol 882: pp 2023.
- [3] Dávila, J. L, Neto, P. I, Noritomi, P. Y, Coelho, R. T, and da Silva, J. V. L. Hybrid Manufacturing: A Review of the Synergy between Directed Energy Deposition and Subtractive Processes. *The International Journal of Advanced Manufacturing Technology*, vol 110(11-12): pp 3377-90, 2020.
- [4] Zhang, W. J, Soshi, M, and Yamazaki, K. Development of an Additive and Subtractive Hybrid Manufacturing Process Planning Strategy of Planar Surface for Productivity and Geometric Accuracy. *The International Journal of Advanced Manufacturing Technology*, vol 109(5-6): pp 1479-91, 2020.
- [5] Basinger, K. L, Keough, C. B, Webster, C. E, Wysk, R. A, Martin, T. M, and Harrysson, O. L. Development of a Modular Computer-Aided Process Planning (Capp) System for Additive-Subtractive Hybrid Manufacturing of Pockets, Holes, and Flat Surfaces. *The International Journal of Advanced Manufacturing Technology*, vol 96(5-8): pp 2407-20, 2018.
- [6] He, Y, Wei, J. C, He, Y. Y, Rong, X. X, Guo, W. F, Wang, F, Wang, Y, and Liu, J. Y. A Process Strategy Planning of Additive-Subtractive Hybrid Manufacturing Based Multi-Dimensional Manufacturability Evaluation of Geometry Feature. *Journal of Manufacturing Systems*, vol 67: pp 296-314, 2023.
- [7] Zhang, S, Zhang, Y. Z, Gao, M, Wang, F. D, Li, Q, and Zeng, X. Y. Effects of Milling Thickness on Wire Deposition Accuracy of Hybrid Additive/Subtractive Manufacturing. *Science and Technology of Welding and Joining*, vol 24(5): pp 375-81, 2019.
- [8] Du, Wei, Bai, Q, and Zhang, B. Machining Characteristics of 18ni-300 Steel in Additive/Subtractive Hybrid Manufacturing. *The International Journal of Advanced Manufacturing Technology*, vol 95(5-8): pp 2509-19, 2017.
- [9] Du, W, Bai, Q, and Zhang, B. A Novel Method for Additive/Subtractive Hybrid Manufacturing of Metallic Parts. *Procedia Manufacturing*, vol 5: pp 1018-30, 2016.
- [10] Feldhausen, T, Raghavan, N, Saleeby, K, Love, L, and Kurfess, T. Mechanical Properties and Microstructure of 316l Stainless Steel Produced by Hybrid Manufacturing. *Journal of Materials Processing Technology*, vol 290: pp 2021.
- [11] Agarwal, S, and Venkateswara, R. P. Predictive Modeling of Force and Power Based on a New Analytical Undeformed Chip Thickness Model in Ceramic Grinding. *International Journal of Machine Tools and Manufacture*, vol 65: pp 68-78, 2013.
- [12] Jiang, G. Y, Yang, H, Xiao, G. J, Zhao, Z. Y, and Wu, Y. Titanium Alloys Surface Integrity of Belt Grinding Considering Different Machining Trajectory Direction. *Frontiers in Materials*, vol 9: pp 1-13, 2022.
- [13] Barry, J, and Byrne, G. The Mechanisms of Chip Formation in Machining Hardened Steels. *Journal of Manufacturing Science and Engineering*, vol 124: pp 528-35, 2002.
- [14] Vayssette, B, Saintier, N, Brugger, C, Elmay, M, and Pessard, E. Surface Roughness of Ti-6al-4v Parts Obtained by Slm and Ebm: Effect on the High Cycle Fatigue Life. *Procedia engineering*, vol 213: pp 89-97, 2018.
- [15] Zhang, Y. C, Li, Z. G, Nie, P. L, and Wu, Y. X. Effect of Ultrarapid Cooling on Microstructure of Laser Cladding In718 Coating. *Surface Engineering*, vol 29(6): pp 414-18, 2013.
- [16] Jiang, Q, Zhang, P. L, Yu, Z. S, Shi, H. C, Li, S. W, Wu, D, Yan, H, Ye, X, and Chen, J. S. Microstructure and Mechanical Properties of Thick Walled Inconel 625 Alloy Manufactured by Wire Arc Additive Manufacture with Different Torch Paths. *Advanced Engineering Materials*, vol 23(1): pp 2020.
- [17] Cui, X, Zhang, S, Zhang, C. H, Chen, J, Zhang, J. B, and Dong, S. Y. Additive Manufacturing of 24crnimo Low Alloy Steel by Selective Laser Melting: Influence of Volumetric Energy Density on Densification, Microstructure and Hardness. *Materials Science and Engineering: A*, vol 809: pp 2021.